Acta Crystallographica Section B
Structural Science
ISSN 0108-7681

Temperature-dependent crystal structure refinement and ^{57}Fe Mössbauer spectroscopy of $Cu_2Fe_2Ge_4O_{13}$

Günther J. Redhammer,[a,b]* Michael Merz,[b] Gerold Tippelt,[a] Karine Sparta,[b] Georg Roth,[b] Werner Treutmann,[c] Werner Lottermoser[a] and Georg Amthauer[a]

[a]Division of Mineralogy, Department of Material Science, University of Salzburg, Hellbrunnerstrasse 34, A-5020 Salzburg, Austria, [b]Institute of Crystallography, RWTH – Aachen, Jägerstrasse 17/19, D-52056 Aachen, Germany, and [c]Institute of Mineralogy, University of Marburg/Lahn, Hans-Meerweinstrasse, D-35032 Marburg/Lahn, Germany

Correspondence e-mail: guenther.redhammer@aon.at

Received 13 February 2006
Accepted 29 November 2006

The germanate compound $Cu_2Fe_2Ge_4O_{13}$, dicopper diiron germanate, was synthesized by solid-state reaction at 1403 K and ambient pressure. There is no change of space-group symmetry between 10 and 900 K. Between 40 K and room temperature the *a* lattice parameter shows a negative thermal expansion which can be connected to a decreasing Cu—Cu interatomic distance. Above room temperature all the lattice parameters are positively correlated with temperature. Among the structural parameters several alterations with temperature occur, which are most prominent for the distorted Fe^{3+} octahedral site. Besides an increase of the average bond length and of the interatomic Fe—Fe distances, distortional parameters also increase with temperature, while the average Cu—O bond length remains almost constant between 100 and 900 K, as do the average Ge—O distances. ^{57}Fe Mössbauer spectroscopy was used to detect long-range magnetic ordering in $Cu_2Fe_2Ge_4O_{13}$. While around 100 K, which is the temperature at which a broad maximum is observed in the magnetic susceptibility, no magnetic ordering was detected in the Mössbauer spectrum, below 40 K a narrow split sextet is developed which is indicative of a three-dimensional magnetic ordering of the sample.

1. Introduction

Over the last few decades, many quantum spin systems have been discovered and investigated intensively, both experimentally and theoretically. These include spin-dimer, spin-Peierls, spin-ladder and spin-plaquet systems. Since these phenomena appear in low-dimensional systems, many efforts have been made to synthesize new materials with low-dimensional structural building units containing spin $\frac{1}{2}$ metal cations. During these investigations germanate–pyroxenes have attracted attention as the clinopyroxene structure, with its infinite zigzag chains of edge-sharing metal–octahedral sites, is a good example of a quasi-one-dimensional structural unit in the true sense (Uchiyama *et al.*, 1999; Völlenke *et al.*, 1967; Hase *et al.*, 1993).

While attempting to synthesize clinopyroxenes in the quaternary system Cu–Fe–Ge–O, a new phase, namely $Cu_2^{2+}Fe_2^{3+}Ge_4O_{13}$, was found and its structure determined (Redhammer & Roth, 2003). Independently from this study and almost at the same time, the compound was also described by Masuda *et al.* (2003). $Cu_2Fe_2Ge_4O_{13}$ contains two magnetically active cations, Fe^{3+} and Cu^{2+}, with $S = 5/2$ and $S = 1/2$, respectively. As shown by Masuda *et al.* (2004, 2005), the material can be described in terms of two magnetic subsystems, one gapped, the other 'gap-less', characterized by two distinct energy scales. Long-range magnetic ordering was

observed at low temperatures (39 K). This ordering is a cooperative phenomenon caused by the weak coupling of these two different spin systems (Masuda *et al.*, 2004). Neutron powder diffraction experiments have been used to solve the magnetic structure below 39 K. It is roughly collinear with the magnetic spins lying in the crystallographic *ac* plane (Masuda *et al.*, 2004, 2005). Recently Redhammer & Roth (2004) also synthesized the Sc^{3+} analogous compound $Cu_2Sc_2Ge_4O_{13}$ and described its crystal structure between 100 and 290 K.

In the present contribution a detailed evaluation of the thermal behaviour of the crystal structure of $Cu_2Fe_2Ge_4O_{13}$ between 15 and 906 K is given. Knowledge of the atomic arrangement at low temperatures is assumed to be essential for any theoretical treatment of the system. Extrapolation of structural features, determined at 298 K, to low (or high) temperatures may not yield the true low-temperature structure even if it is assumed that no phase transitions occur. For example, in the isotypic and isostructural compound $Cu_2Sc_2Ge_4O_{13}$ an obvious increase of the *a* lattice parameter in conjunction with an increase of the shortest Cu—Cu interatomic contact was found with decreasing temperature (Redhammer & Roth, 2004). Another aim of the study is to further characterize $Cu_2Fe_2Ge_4O_{13}$ at low temperature using ^{57}Fe Mössbauer spectroscopy. Using this kind of spectroscopy allows a 'direct' analysis of the behaviour of the Fe^{3+} sublattice, which is of special interest to shed additional light on the magnetic transitions observed in the magnetic susceptibilities at ~100 and 40 K.

2. Experimental

2.1. Material synthesis

Single crystals of the title compound were synthesized at ambient pressure and oxygen fugacity within a temperature range between 1173 and 1403 K. The starting material of the synthesis was a stoichiometric homogeneous mixture of CuO, Fe_2O_3 and GeO_2. This oxide mixture was pressed into pellets, put into an open platinum crucible, covered with a lid and transferred to a high-temperature resistance furnace. The first heating steps were performed in the range 1173–1223 K, well below the reduction reaction $Cu^{2+}O \rightarrow Cu^{+}{}_2O$ at 1293 K (Breuer *et al.*, 1983). Within a few days, the black-coloured starting material transformed to a blue–green reaction product, which contained a mixture of $CuGeO_3$ and the title compound. Raising the temperature to 1323 K drastically reduced the amount of the impurity phase $CuGeO_3$, and in subsequent heating sequences at 1373 K a pure and homogeneous sample of the title compound was obtained. The total synthesis time was 67 d. A small amount of the powder sample (25 mg) was used to determine the magnetic susceptibility using a Quantum Design SQUID magnetometer. The obtained susceptibility is similar to that observed and described by Masuda *et al.* (2004, 2005), showing a broad maximum at *ca* T = 100 K, which is followed by a three-dimensional ordered phase below T_N = 39 K. Thus, it is assumed that the magnetic characteristics of the sample, studied here, coincide extremely well with those described by Masuda *et al.* (2004, 2005). A small part of the powder sample was heated at 1403 K for another 72 h, yielding short prismatic to cuboid pale-green crystals, which were suitable for single-crystal X-ray diffraction.

2.2. Single-crystal X-ray diffraction

A pale green crystal of $Cu_2Fe_2Ge_4O_{13}$ was used for single-crystal X-ray diffraction experiments. Intensity data sets between 90 and 290 K were collected on a Stoe IPDS II imaging-plate diffractometer system (Mo $K\alpha$ radiation, pyrolytic graphite monochromator), equipped with a cryostream liquid N_2 cryostat (85–300 K, an accuracy of at least 1 K). Intensity data were collected to 65.0° in 2θ within an ω range of 0–180° and two different φ positions in most cases; the ω rotation during exposure was 1.5° per frame. The high-temperature experiments (298–906 K) were performed on a Stoe IPDS I image plate diffractometer system, equipped with an in-house built heating device. Owing to the geometry of the heating device, only a limited ω range (60–210°) was accessible, giving rise to a low completeness of data with an average coverage of ~ 90%. Data were measured from low to high temperatures. Lattice parameters determined from single-crystal X-ray diffraction data agree well with those determined from X-ray powder diffraction. Absorption correction was carried out empirically *via* symmetry equivalents using the *SHAPE* software (Stoe & Cie, 1996). Structure solution (using Patterson methods) and subsequent refinement were carried out with the programs *SHELXS*97 and *SHELXL*97 (Sheldrick, 1997), as implemented in the program suite *WinGX*1.64 (Farrugia, 1999). X-ray scattering factors in their ionic form, together with anomalous dispersion coefficients, were taken from the *International Tables for Crystallography* (Wilson, 1992). Structure drawings were prepared using the *DIAMOND*3.0 program (Bradenburg & Berndt, 1999).

2.3. X-ray powder diffraction and thermal expansion tensor

To obtain detailed information on the temperature variation of the lattice parameters, X-ray powder diffraction measurements (10–110° in 2Θ, continuous scan) were carried out in the temperature range 10–873 K. Low-temperature data (10–298 K) were collected at the Institute of Crystallography, RWTH Aachen, on a Philips X'Pert diffractometer equipped with a Janis CCS-250 cryostat [Bragg–Brentano geometry, Cu $K\alpha$ radiation, primary and secondary-side 0.04 rad soller slits, secondary-side position-sensitive X'Celerator (PANalytical) detector]. High-temperature data were collected at the University of Salzburg on a Philips X'Pert diffractometer system, equipped with an Anton PAAR HTK-16 high-temperature chamber (Cu $K\alpha$ radiation, primary- and secondary-side 0.04 rad soller slits, secondary-side graphite monochromator). Lattice parameters were extracted from Rietveld refinements based on the powder data using the *FULLPROF* program (Rodrigues-Carvajal, 2001). Silicon was used as an internal standard in both cases.

Table 1
Data collection parameters and results of structure refinement for $Cu_2Fe_2Ge_4O_{13}$ at selected temperatures.

	90 K	298 K	362 K	611 K	903 K
Crystal data					
Chemical formula	$Cu_2Fe_2Ge_4O_{13}$	$Cu_2Fe_2Ge_4O_{13}$	$Cu_2Fe_2Ge_4O_{13}$	$Cu_2Fe_2Ge_4O_{13}$	$Cu_2Fe_2Ge_4O_{13}$
M_r	737.14	737.14	737.14	737.14	737.14
Cell setting, space group	Monoclinic, $P2_1/m$	Monoclinic, $P2_1/m$	Monoclinic, $P2_1/m$	Monoclinic, $P2_1/m$	Monoclinic, $P2_1/m$
Temperature (K)	90 (2)	298 (2)	362 (2)	611 (2)	903 (2)
a, b, c (Å)	12.090 (2), 8.4901 (9), 4.8626 (8)	12.088 (2), 8.5019 (9), 4.8703 (8)	12.0883 (8), 8.5076 (7), 4.8727 (5)	12.1011 (8), 8.5290 (7), 4.8841 (5)	12.1165 (8), 8.5535 (7), 4.8974 (5)
β (°)	96.13 (2)	96.17 (2)	96.18 (2)	96.24 (2)	96.326 (11)
V (Å^3)	496.27 (13)	497.61 (13)	498.21 (8)	501.10 (8)	504.47 (7)
Z	2	2	2	2	2
D_x (Mg m^{-3})	4.933	4.920	4.915	4.885	4.853
Radiation type	Mo $K\alpha$	Mo $K\alpha$	Mo $K\alpha$	Mo $K\alpha$	Mo $K\alpha$
μ (mm^{-1})	19.05	18.99	18.98	18.87	18.75
Crystal form, colour	Prismatic, pale green	Prismatic, pale green	Prismatic, pale green	Prismatic, pale green	Prismatic, pale green
Crystal size (mm)	0.12 × 0.11 × 0.08	0.12 × 0.11 × 0.08	0.12 × 0.11 × 0.08	0.12 × 0.11 × 0.08	0.12 × 0.11 × 0.08
Data collection					
Diffractometer	Stoe IPDS-II	Stoe IPDS-I	Stoe IPDS-I	Stoe IPDS-I	Stoe IPDS-I
Data collection method	Rotation method, ω	Rotation method, φ	Rotation method, φ	Rotation method, φ	Rotation method, φ
Absorption correction	Numerical	Numerical	Numerical	Numerical	Numerical
T_{min}	0.12	0.12	0.12	0.12	0.12
T_{max}	0.25	0.25	0.25	0.25	0.25
No. of measured, independent and observed reflections	5776, 1527, 1202	4906, 1267, 1087	4515, 1164, 956	4515, 1165, 914	4491, 1155, 699
Criterion for observed reflections	$I > 2\sigma(I)$	$I > 2\sigma(I)$	$I > 2\sigma(I)$	$I > 2\sigma(I)$	$I > 2\sigma(I)$
R_{int}	0.060	0.039	0.049	0.046	0.127
θ_{max} (°)	30.0	28.1	28.0	27.9	27.9
Refinement					
Refinement on	F^2	F^2	F^2	F^2	F^2
$R[F^2 > 2\sigma(F^2)]$, $wR(F^2)$, S	0.032, 0.058, 1.01	0.021, 0.048, 1.02	0.027, 0.053, 0.97	0.028, 0.062, 0.99	0.058, 0.136, 0.97
No. of reflections	1527	1267	1164	1165	1155
No. of parameters	110	107	110	110	110
H-atom treatment	No H atoms present	No H atoms present	No H atoms present	No H atoms present	No H atoms present
Weighting scheme	$w = 1/[\sigma^2(F_o^2) + (0.0238P)^2]$, where $P = (F_o^2 + 2F_c^2)/3$	$w = 1/[\sigma^2(F_o^2) + (0.0291P)^2]$, where $P = (F_o^2 + 2F_c^2)/3$	$w = 1/[\sigma^2(F_o^2) + (0.0286P)^2]$, where $P = (F_o^2 + 2F_c^2)/3$	$w = 1/[\sigma^2(F_o^2) + (0.0335P)^2]$, where $P = (F_o^2 + 2F_c^2)/3$	$w = 1/[\sigma^2(F_o^2) + (0.0648P)^2]$, where $P = (F_o^2 + 2F_c^2)/3$
$(\Delta/\sigma)_{max}$	0.001	0.001	< 0.0001	0.001	< 0.0001
$\Delta\rho_{max}$, $\Delta\rho_{min}$ (e Å^{-3})	1.51, −1.16	1.45, −1.59	1.16, −0.85	0.83, −0.90	1.74, −1.93
Extinction method	*SHELXL*	*SHELXL*	*SHELXL*	*SHELXL*	*SHELXL*
Extinction coefficient	0.0024 (3)	0.0332 (9)	0.0242 (8)	0.0211 (9)	0.055 (3)

Computer programs used: *Stoe X-Area* (Stoe & Cie, 2002), *SHELXS*97 (Sheldrick, 1997), *SHELXL*97 (Sheldrick, 1997), *DIAMOND*3.0 (Bradenburg & Berndt (1999), *WINGX*1.70.00 (Farrugia, 1999).

In order to parameterize the cell parameters of $Cu_2Fe_2Ge_4O_{13}$ for subsequent thermal expansion tensor calculations, they were fitted with polynomial functions of the order 6 for b, 4 for c and 7 for β over the whole temperature range. Because of the more complicated behaviour of a, we used a seventh-order polynomial fit between 10 K and room temperature and a fifth-order polynomial fit above room temperature for a. Regression coefficients were better than 0.998 for all refinements and reproduced extremely well the trends both at low and high temperatures. The Lagrangian coefficients of the thermal expansion tensor α_{ij} were calculated for the conventional orthonormal basis $\boldsymbol{e_2}\|\boldsymbol{b}^*\|\boldsymbol{b}, \boldsymbol{e_3}\|\boldsymbol{c}$ and $\boldsymbol{e_1}\|\boldsymbol{e_2} \times \boldsymbol{e_3}\|\boldsymbol{a}^*$, with the 300 K values for a_0, b_0, c_0 and β_0, using

$$\alpha_{11} = \frac{1}{a_0 \sin\beta_0}\left[\sin\beta\frac{da}{dT} + a\cos\beta\frac{d\beta}{dT}\right]$$

$$\alpha_{22}(T) = \frac{1}{b_0}\frac{db}{dT}$$

$$\alpha_{33}(T) = \frac{1}{c_0}\frac{dc}{dT}$$

$$\alpha_{13}(T) = \frac{1}{a_0}\frac{da}{dT}\left[\frac{1}{\sin 2\beta_0} - \frac{\sin\beta}{2\cos\beta_0}\right] - \frac{a\cos\beta}{2a_0\cos\beta_0}\frac{d\beta}{dT} - \frac{\cot\beta_0}{2c_0}\frac{dc}{dT},$$

with b as the unique axis (Schlenker *et al.*, 1975; Knight et *al.*, 1999; Schonfield *et al.*, 2004). The diagonalization of the α_{ij} tensor leads to the eigenvalues $\alpha_1(T) = \frac{1}{2}(\alpha_{11} + \alpha_{33}) - r_m$ and $\alpha_3(T) = \frac{1}{2}(\alpha_{11} + \alpha_{33}) + r_m$, where $r_m^2 = \frac{1}{4}(\alpha_{33} - \alpha_{11})^2 + \alpha_{13}^2$ is

Table 2
Selected bond lengths (Å), bond angles (°), interatomic distances (Å) and distortion parameters for $Cu_2Fe_2Ge_4O_{13}$ at different temperatures.

	90 K	298 K	362 K	611 K	903 K	Change (%)†
Fe—O6	1.953 (3)	1.955 (2)	1.958 (2)	1.955 (3)	1.956 (7)	0.16
Fe—O7	2.007 (3)	2.004 (2)	2.007 (2)	2.009 (4)	2.009 (7)	0.14
Fe—O8	2.047 (3)	2.053 (2)	2.054 (3)	2.061 (4)	2.074 (7)	1.33
Fe—O1	2.050 (3)	2.059 (2)	2.060 (3)	2.064 (4)	2.073 (6)	1.12
Fe—O4	2.038 (3)	2.037 (2)	2.035 (3)	2.037 (4)	2.047 (6)	0.41
Fe—O6	2.083 (3)	2.088 (2)	2.094 (3)	2.106 (4)	2.125 (7)	2.01
⟨Fe—O⟩	2.030	2.033	2.035	2.039	2.047	0.87
BLD (%)	1.63 (5)	1.75 (5)	1.72 (5)	1.88 (5)	2.11 (5)	28.98
ELD (%)	9.67 (5)	9.61 (5)	9.66 (5)	9.65 (5)	9.54 (5)	−1.31
e_u/e_s	1.211	1.207	1.206	1.206	1.204	−0.52
OAV (°)	198.0 (2)	196.3 (2)	196.3 (2)	196.3 (2)	193.9 (2)	−2.07
Volume (Å^3)	10.31 (1)	10.36 (1)	10.39 (1)	10.45 (1)	10.58 (1)	2.58
Cu—O9	1.929 (3)	1.925 (2)	1.922 (3)	1.919 (4)	1.915 (8)	−0.74
Cu—O4	1.931 (3)	1.933 (2)	1.939 (3)	1.939 (4)	1.940 (8)	0.48
Cu—O9	1.951 (3)	1.952 (2)	1.949 (3)	1.947 (4)	1.944 (7)	−0.38
Cu—O9	1.998 (3)	2.005 (2)	2.004 (3)	2.009 (4)	2.015 (7)	0.89
⟨Cu—O⟩	1.953	1.954	1.954	1.953	1.954	0.07
BLD (%)	1.17 (5)	1.31 (5)	1.30 (5)	1.41 (5)	1.59 (5)	35.98
Cu—Cu	3.035 (1)	3.021 (1)	3.019 (1)	3.013 (1)	3.017 (3)	−0.54
Cu—Fe	3.071 (1)	3.072 (1)	3.074 (1)	3.079 (1)	3.079 (2)	0.26
Fe—Fe	3.201 (1)	3.208 (1)	3.209 (1)	3.216 (1)	3.226 (2)	0.78
Fe—Fe	3.256 (1)	3.258 (1)	3.259 (1)	3.269 (1)	3.282 (2)	0.80
Cu—O9—Cu	102.87 (12)	102.4 (2)	102.5 (2)	102.4 (2)	102.9 (2)	0.00
Fe—O6—Fe	107.47 (13)	107.3 (2)	107.1 (2)	107.1 (2)	107.1 (2)	
Fe—O1—Fe	102.66 (13)	102.4 (2)	102.3 (2)	102.3 (2)	102.5 (2)	
Ge1—O1	1.748 (4)	1.740 (3)	1.746 (4)	1.749 (5)	1.750 (7)	0.15
Ge1—O4 ×2	1.748 (3)	1.748 (2)	1.748 (3)	1.751 (3)	1.750 (9)	0.21
Ge1—O3	1.769 (4)	1.772 (3)	1.771 (4)	1.770 (5)	1.776 (10)	0.40
⟨Ge1—O⟩ (Å)	1.753	1.752	1.753	1.755	1.758	0.24
O1—O3	2.666	2.655	2.669	2.668	2.669	0.10
O4—O4	2.825	2.826	2.827	2.834	2.848	0.83
BLD (%)	0.46 (5)	0.57 (5)	0.52 (5)	0.43 (5)	0.53 (5)	18.12
TAV (°)	35.6 (2)	38.5 (2)	34.6 (2)	35.9 (2)	33.7 (2)	−5.23
TQE	1.0091	1.0098	1.0088	1.0092	1.0088	−0.03
Volume (Å^3)	2.73 (1)	2.72 (1)	2.73 (1)	2.74 (1)	2.73 (1)	−0.03
Ge2—O2	1.702 (5)	1.699 (3)	1.694 (5)	1.689 (4)	1.684 (12)	−1.04
Ge2—O7 ×2	1.746 (3)	1.746 (2)	1.746 (3)	1.748 (4)	1.747 (7)	−0.03
Ge2—O5	1.777 (4)	1.781 (3)	1.776 (4)	1.778 (5)	1.777 (10)	−0.03
⟨Ge2—O⟩	1.743	1.743	1.741	1.741	1.738	−0.28
O5—O2	2.644	2.656	2.646	2.657	2.671	0.99
O7—O7	2.880	2.886	2.886	2.886	2.883	0.13
BLD (%)	1.18 (5)	1.26 (5)	1.34 (5)	1.48 (5)	1.55 (5)	31.73
TAV (°)	29.6 (2)	26.9 (2)	27.4 (2)	24.2 (2)	20.0 (2)	−32.42
TQE	1.0080	1.0073	1.0073	1.0067	1.0057	−0.23
Volume (Å^3)	2.69 (1)	2.69 (1)	2.68 (1)	2.68 (1)	2.67 (1)	−0.49
Ge3—O9 ×2	1.737 (3)	1.734 (2)	1.735 (3)	1.737 (4)	1.741 (10)	0.21
Ge3—O3	1.750 (4)	1.747 (3)	1.747 (4)	1.747 (5)	1.743 (9)	−0.36
Ge3—O5	1.758 (4)	1.748 (3)	1.757 (4)	1.755 (5)	1.754 (11)	−0.23
⟨Ge3—O⟩	1.745	1.741	1.743	1.744	1.744	−0.04
O3—O5	2.904	2.894	2.901	2.905	2.914	0.36
O9—O9	2.843	2.841	2.839	2.839	2.824	−0.66
BLD (%)	0.51 (5)	0.39 (5)	0.49 (5)	0.41 (5)	0.26 (5)	−45.36
TAV (°)	1.4 (2)	1.6 (2)	1.5 (2)	1.8 (2)	2.9 (2)	105.72
TQE	1.0004	1.0005	1.0005	1.0005	1.0008	0.04
Volume (Å^3)	2.73 (1)	2.70 (1)	2.72 (1)	2.72 (1)	2.72 (1)	−0.23
Ge4—O2	1.733 (3)	1.728 (3)	1.729 (4)	1.725 (5)	1.720 (10)	−0.78
Ge4—O8	1.747 (2)	1.744 (2)	1.743 (5)	1.745 (5)	1.741 (10)	−0.31
Ge4—O6 ×2	1.756 (2)	1.753 (2)	1.750 (4)	1.751 (4)	1.749 (7)	−0.43
⟨Ge4—O⟩ (Å)	1.748	1.745	1.743	1.743	1.739	−0.49
O2—O8	2.863	2.848	2.842	2.826	2.797	−2.28
O6—O6	2.991	2.984	2.978	1.977	2.962	−0.99
BLD (%)	0.44 (5)	0.49 (5)	0.38 (5)	0.51 (5)	0.57 (5)	26.48
TAV (°)	62.6 (2)	59.8 (2)	58.9 (2)	56.4 (2)	54.4 (2)	−8.23
TQE	1.0184	1.0177	1.0173	1.0168	1.0164	−0.20

the radius of the Mohr circle. The φ angle between the eigenvector $\boldsymbol{a_1}$ and the $\boldsymbol{a}^*$ direction is obtained using the relation
$\tan\varphi(T) = -(\alpha_{33} - \alpha_{11} - 2r_m)/2\alpha_{13}$ (Paufler, 1997).

2.4. ^{57}Fe Mössbauer spectroscopy

Transmission ^{57}Fe Mössbauer spectra between 20 and 300 K were collected using a Mössbauer apparatus in a horizontal arrangement (^{57}Co/Rh single-line thin source, constant acceleration, symmetric triangular velocity shape, multi-channel analyser with 1024 channels and velocity calibration to α-Fe). The Mössbauer spectrometer was equipped with a vaporizer–cryostat for low-temperature measurements. One measurement was performed for temperatures $T < 80$ K (using liquid He as a cooling medium). The folded spectra were analysed using Lorentzian-shaped doublets or sextets using a full-static Hamiltonian approach.

In most of the figures, regression lines where fitted to the data to clarify trends. Except Fig. 3, these regressions correspond to polynomials of first (linear) or second (quadratic) order: $y = a_o + a_1{*}x + a_2{*}x^2$. Second-order polynomial functions were used, when obvious curvatures were visible in the data. Regression fit values were above 0.9 in almost all fits. These fits are purely mathematical in nature and should serve as guides to the eye only as they have no physical meaning.

3. Results and discussion

Analysis of systematic absences and intensity statistics indicated the space group $P2_1/m$ for the title compound within the whole temperature range investigated by single-crystal X-ray diffraction (90–900 K). Special care was taken to look for weak superstructure reflections in the low-temperature data; however, no weak superstructure develops below room temperature, as might have been expected from the behaviour of lattice parameters (see below). Full-matrix least-squares refinements based on F^2 using anisotropic atomic displacement

Table 2 (continued)

	90 K	298 K	362 K	611 K	903 K	Change (%)†
Volume (Å^3)	2.67 (1)	2.66 (1)	2.65 (1)	2.65 (1)	2.64 (1)	−1.21

† Change of parameter between 90 K and 903 K expressed in percent relative to the value at 90 K:

$$\mathrm{BLD} = \frac{100}{n}\sum_{i=1}^{n}\frac{|(X-\mathrm{O})_i - \langle(X-\mathrm{O})\rangle|}{\langle(X-\mathrm{O})\rangle}\%,$$

n = amount of cation–anion bonds and $X-\mathrm{O}$ = cation–anion (oxygen) distance (Renner & Lehmann, 1986);

$$\mathrm{ELD} = \frac{100}{n}\sum_{i=1}^{n}\frac{|(\mathrm{O}-\mathrm{O})_i - \langle(\mathrm{O}-\mathrm{O})\rangle|}{\langle(\mathrm{O}-\mathrm{O})\rangle}\%,$$

n = amount of edges and (O—O) = oxygen–oxygen interatomic distance defining an edge of the octahedron (Renner & Lehmann, 1986);

$$\mathrm{OAV} = \sum_{i=1}^{12}(\Theta_i - 90^\circ)^2/11$$

with Θ_i = O—M—O bonding angle (Robinson *et al.*, 1971);

$$\mathrm{TAV} = \sum_{i=1}^{6}(\Theta_i - 109.57^\circ)^2/5$$

with Θ_i = O—T—O bonding angle (Robinson *et al.*, 1971).

parameters easily converged to $R_1 < 0.035$ for all data sets. Table 1 contains a summary of the experimental conditions during data collection and structural refinement parameters at selected temperatures; the refined fractional atomic coordinates and equivalent isotropic displacement parameters have been deposited.[1] The anisotropic displacement parameters have been deposited in the crystallographic information file (CIF), together with the complete set of single-crystal data for all the 17 temperatures investigated. Atomic displacement parameters increase almost linearly with temperature. There is no abnormal behaviour in the thermal motion of any atoms at low temperature which would be indicative of a phase transition. Generally atomic motion becomes more anisotropic with temperature. This is most evident for the Cu and for the O9 atom, which is bonded to two Cu^{2+} sites. These two are obviously anisotropic at high temperatures. Table 2 compiles selected bond lengths, bond angles and distortional parameters, while Table 3 contains the full set of lattice parameters for $Cu_2Fe_2Ge_4O_{13}$ between 10 and 906 K.

The powder diffraction data, collected at low temperatures (10 K to room temperature), were successfully indexed within the space group $P2_1/m$. Between 10 K and room temperature neither extra reflections nor any broadening or splitting of the diffraction lines were detected in our powder diffraction diagrams, even if we assume a small half-width of the diffraction lines (smaller than 0.007°). Furthermore, our single-crystal X-ray data did not show any reflections violating $P2_1/m$ symmetry. Thus, we conclude that the $P2_1/m$ symmetry is retained even at low temperatures throughout the magnetic phase transition at 39 K. Any discontinuities in lattice parameters have to be ascribed to changes of the structural topology without change of symmetry. Our findings agree with those of Masuda *et al.* (2004) who stated that besides the magnetic phase transition at 40 K no other transition is present in the 1.5–300 K range. Structural details (bond lengths and angles) extracted from the Rietveld refinements are in the range of parameters obtained from single-crystal data, however, the spread of data as a function of temperature is large and generally no clear and smooth variations with T are observable. Thus, only structural data from single-crystal structure refinement are discussed in detail.

3.1. $Cu_2Fe_2Ge_4O_{13}$ at room temperature

The structure of the title compound is isotypic to $Cu_2Sc_2Ge_4O_{13}$. Its structural topology was described in great detail in Redhammer & Roth (2004). Thus, only a basic description of $Cu_2Fe_2Ge_4O_{13}$ will be given here. The title compound consists of three main building units (Fig. 1). These are infinite chains of edge-sharing Fe^{3+} octahedra, running parallel to the crystallographic b axis and displaying an obvious one-dimensional character. Choosing the O4—Fe—O6 direction as the apex–cation–apex axis of the octahedron individual octahedra show a *cis–trans* connection. The crankshaft-like Fe^{3+} chains are interconnected along the a axis by Cu^{2+} dimers, thereby forming a slightly buckled cation sheet of Fe^{3+} and Cu^{2+} sites within the ab plane. Along c these

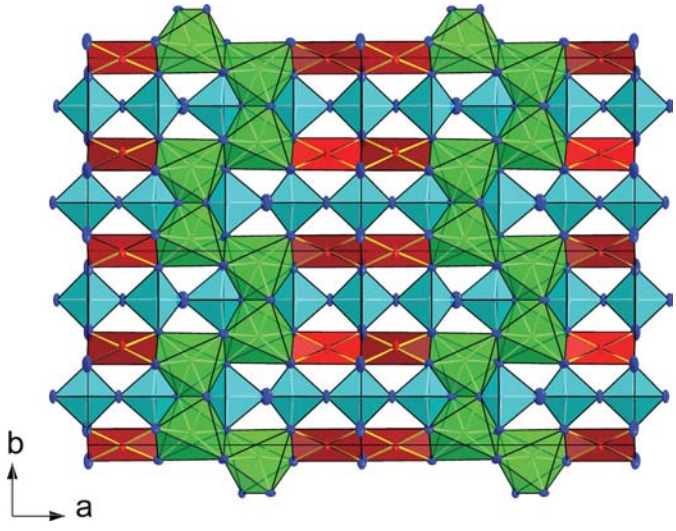

Figure 1
Polyhedral representation of the $Cu_2Fe_2Ge_4O_{13}$ structure viewed normal to (001).

[1] Supplementary data for this paper are available from the IUCr electronic archives (Reference: WS5044). Services for accessing these data are described at the back of the journal.

Table 3
Lattice parameters (Å, °) for $Cu_2Fe_2Ge_4O_{13}$ as a function of temperature.

SC = single-crystal data; RR = Rietveld refinement data; standard uncertainties are smaller than 0.0012 Å for *a*, 0.0009 Å for *b*, 0.0007 Å for *c* and smaller than 0.0014 Å for the monoclinic angle *β*.

T (K)	*a* (Å)	*b* (Å)	*c* (Å)	*β* (Å)	*V* (Å^3)	
10	12.0934	8.4889	4.8606	96.137	496.130	RR
20	12.0934	8.4889	4.8606	96.135	496.127	RR
30	12.0932	8.4890	4.8612	96.135	496.184	RR
36	12.0929	8.4892	4.8613	96.134	496.193	RR
45	12.0923	8.4892	4.8619	96.134	496.234	RR
60	12.0914	8.4894	4.8622	96.132	496.245	RR
70	12.0910	8.4895	4.8623	96.132	496.241	RR
80	12.0907	8.4899	4.8629	96.134	496.313	RR
90	12.0901	8.4901	4.8626	96.131	496.272	SC
100	12.0895	8.4903	4.8636	96.135	496.363	RR
110	12.0890	8.4906	4.8636	96.134	496.361	RR
130	12.0881	8.4914	4.8644	96.137	496.444	SC
135	12.0880	8.4918	4.8647	96.137	496.487	RR
150	12.0874	8.4922	4.8649	96.141	496.508	RR
170	12.0867	8.4931	4.8657	96.139	496.617	SC
175	12.0867	8.4937	4.8659	96.144	496.665	RR
200	12.0859	8.4947	4.8667	96.143	496.776	SC
210	12.0862	8.4960	4.8671	96.150	496.900	RR
230	12.0857	8.4972	4.8677	96.153	497.010	RR
250	12.0858	8.4979	4.8691	96.161	497.187	SC
250	12.0861	8.4986	4.8686	96.156	497.194	RR
270	12.0857	8.5003	4.8695	96.161	497.364	RR
290	12.0861	8.5008	4.8704	96.167	497.497	SC
298	12.0864	8.5021	4.8703	96.167	497.575	RR
298	12.0866	8.5019	4.8703	96.168	497.571	RR
303	12.0868	8.5022	4.8702	96.168	497.581	RR
320	12.0876	8.5043	4.8715	96.171	497.872	SC
323	12.0872	8.5039	4.8711	96.169	497.794	RR
343	12.0878	8.5057	4.8720	96.178	498.004	RR
362	12.0883	8.5076	4.8727	96.177	498.211	SC
363	12.0893	8.5082	4.8728	96.178	498.300	RR
383	12.0899	8.5096	4.8737	96.185	498.482	RR
403	12.0912	8.5118	4.8745	96.191	498.750	RR
423	12.0921	8.5111	4.8748	96.196	498.765	RR
423	12.0919	8.5126	4.8756	96.197	498.929	RR
445	12.0943	8.5142	4.8763	96.207	499.185	SC
473	12.0949	8.5170	4.8776	96.212	499.506	RR
473	12.0943	8.5172	4.8774	96.214	499.469	RR
523	12.0967	8.5218	4.8798	96.225	500.070	RR
523	12.0968	8.5215	4.8799	96.227	500.060	RR
528	12.0971	8.5205	4.8803	96.221	500.067	SC
573	12.0987	8.5259	4.8823	96.237	500.637	RR
611	12.1011	8.5290	4.8841	96.245	501.098	SC
623	12.1017	8.5295	4.8844	96.247	501.176	RR
673	12.1034	8.5338	4.8863	96.267	501.684	RR
695	12.1039	8.5353	4.8886	96.279	502.014	SC
723	12.1064	8.5376	4.8887	96.283	502.262	RR
736	12.1073	8.5380	4.8899	96.281	502.445	SC
773	12.1090	8.5421	4.8910	96.297	502.854	RR
778	12.1083	8.5422	4.8916	96.295	502.895	SC
819	12.1105	8.5453	4.8931	96.307	503.312	SC
823	12.1115	8.5458	4.8932	96.311	503.388	RR
873	12.1139	8.5504	4.8963	96.322	504.072	RR
903	12.1165	8.5535	4.8974	96.326	504.469	SC

sheets are separated by small chains of four corner-sharing and symmetrically distinct GeO_4 tetrahedra. These Ge_4O_{13} units are aligned parallel to the crystallographic *a* axis, perpendicular to *b* and are slightly bent.

The Fe^{3+} octahedron clearly deviates from ideal geometry, however, structural parameters found here are in excellent agreement with the data of Masuda *et al.* (2003). While the individual Fe^{3+}—O bond lengths are quite uniform, the O—O edge lengths are diverse, expressed by the high value of ELD (= deviation of individual edge length from their mean value; Renner & Lehmann, 1986). The ratio e_u/e_s (with e_u = average of unshared and e_s = average of shared edges) is a measure of polyhedral distortion (Toraya, 1981). For the title compound e_u/e_s for the $Fe^{3+}O_6$ octahedron is 1.21; this is comparable to the Sc^{3+} analogue. Typical values for regular $Fe^{3+}O_6$ octahedra, however, are between 1.03 and 1.10 (Redhammer & Roth, 2004). The octahedral angle variance (OAV; Robinson *et al.*, 1971) also is unusually high and supports the argument of an extreme distortion of the $Fe^{3+}O_6$ octahedron (Table 3).

The Cu^{2+} cation is in a true fourfold coordination with four bond lengths within the range 1.925 (3)–2.000 (3) Å. These four bonds correspond to the equatorial bond lengths $\langle M—O\rangle_{eq}$ within an octahedron. The next-nearest O atoms are 2.828 (3) and 2.890 (3) Å away and are considered as non-bonding. It is well understood that this distortion of the Cu^{2+} site is due to the specific electronic nature of Cu^{2+} with its partly filled *d* orbitals. Transition metal cations having such a degenerate electronic state will undergo a Jahn–Teller distortion to a system with lower symmetry, thereby partly removing the degeneracy (*e.g.* Benabbas, 2006; Burns & Hawthorne, 1996). For sixfold coordination the degeneracy is generally removed by a strong tetragonal elongation of the Cu^{2+} octahedra. The average Cu—O bond length in $Cu_2Fe_2Ge_4O_{13}$ corresponds well to the average $\langle Cu^{2+}—O_{eq}\rangle$ bond length found by Burns & Hawthorne (1996) in investigating the geometry of 159 symmetrically unique (4 + 2)-distorted $Cu^{2+}O_6$ octahedra in 90 different Cu^{2+} oxysalt minerals. According to Burns & Hawthorne (1996) the average $\langle Cu^{2+}—O_{eq}\rangle$ is 1.973 Å with a standard deviation of 0.048 Å, while the average distance of the two next-nearest O atoms $\langle Cu^{2+}—O_{aq}\rangle$ is 2.505 Å with a standard deviation of 0.205 Å. The latter value is clearly smaller than that found for the title compound and it is thus concluded that the Cu^{2+} site is described by a fourfold rather than 4 + 2-fold coordination.

The structural data for the Cu^{2+} site found here are in excellent agreement with those reported by Masuda *et al.*

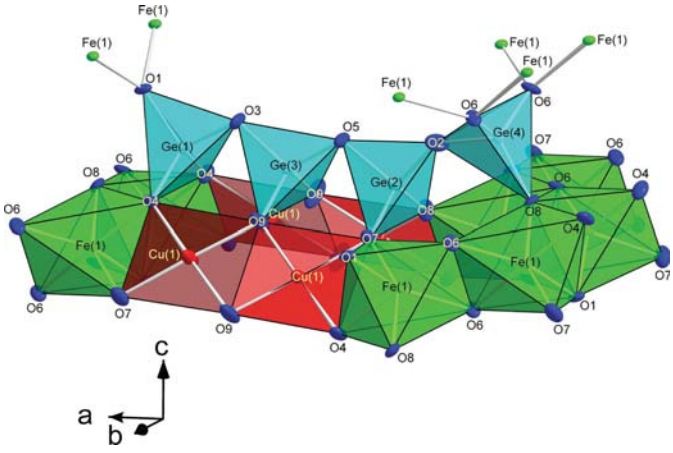

Figure 2
Polyhedral representation of the GeO_4 tetramer and its interconnection with the $Fe^{3+}O_6$ octahedra and the CuO_4 plane. Displacement ellipsoids are plotted at the 95% probability level.

(2003). Also, the Cu—O bonds are similar to those in $Cu_2Sc_2Ge_4O_{13}$ (Redhammer & Roth, 2004). Two sets of Cu planes are connected to each other *via* the common O9—O9 edge forming a Cu–Cu dimer. Compared with $Cu_2Sc_2Ge_4O_{13}$, this O9—O9 edge is somewhat shorter, but on the other hand the Cu–Cu interatomic distance, which is parallel to the crystallographic *a* axis, is longer in $Cu_2Fe_2Ge_4O_{13}$, which may be seen as an indication for a larger repulsion between the Cu–Cu pair. The Cu dimer shares two of its edges with the crankshaft-like $Fe^{3+}O_6$ chains, thus bridging them in the *a* direction. They are also inclined with respect to the *a* axis and the inclination alters along the $+b$ and $-b$ direction (Fig. 2).

The average Ge—O bond lengths range between 1.742 (3) and 1.754 (3) Å at room temperature and compare well with those of Masuda *et al.* (2003) and Redhammer & Roth (2004). The oligomer of GeO_4 tetrahedra is less bent in $Cu_2Fe_2Ge_4O_{13}$ compared with the Sc analogue. This is mainly due to the much larger O5—O2—O8 tetrahedral bridging angle of 149.9 (1)°. While the Ge1 tetrahedron is the largest and displays obvious tetrahedral angle variance (Robinson *et al.*, 1971), the $Ge3O_4$ site, which is connected to the $Ge1O_4$ tetrahedron *via* the common O3 atom, is the most regular one (Table 3). The observation holds true that the more common corners a GeO_4 site must share with the $Fe^{3+}O_6$ chain, the more distorted it is. The $Ge4O_4$ tetrahedron, which has the largest number of common corners with two Fe^{3+} chains (namely three), displays the largest tetrahedral distortion (Fig. 2, Table 3).

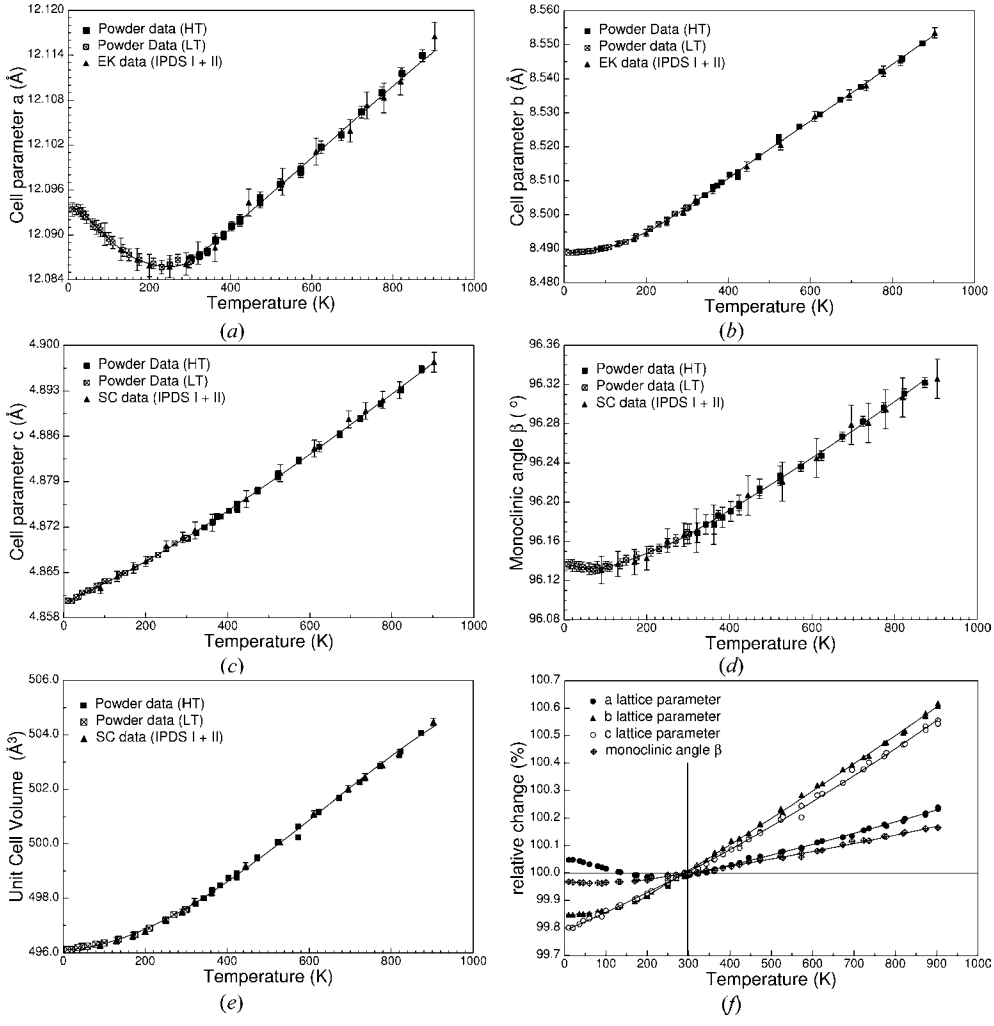

Figure 3
Unit-cell parameters of $Cu_2Fe_2Ge_4O_{13}$ as a function of temperature (*a*)–(*e*); in (*f*) the changes of unit-cell parameters relative to the value at room temperature are shown; if not visible, error bars are smaller than the symbol.

3.2. $Cu_2Fe_2Ge_4O_{13}$ between 10 and 900 K

3.2.1. Lattice parameters. For $Cu_2Sc_2Ge_4O_{13}$, Redhammer & Roth (2004) observed a decrease of the *a* lattice parameter with increasing temperature (negative thermal expansion), while the other lattice parameters were positively correlated with temperature. However, no data are available for the Sc^{3+} compound for $T >$ room temperature. The question arises whether this nega-

Table 4
(Top) Coefficients α_{ij} (10^{-6} K^{-1}) of the thermal expansion tensor of $Cu_2Fe_2Ge_4O_{13}$ for selected temperature intervals (bottom).

Eigenvalues α_1 and α_3 in 10^{-6} K^{-1} ($\alpha_2 = \alpha_{22}$) and angles between the eigenvectors e_1, e_3 of the thermal expansion tensor and the orthogonal crystal axes a^*, b and c.

ΔT (K)	α_{11}	α_{22}	α_{33}	α_{13}
10–20	−1.1 (3)	0.5 (3)	6.1 (3)	1.6 (3)
36–45	−3.5 (3)	1.3 (3)	6.3 (3)	1.1 (3)
70–80	−4.6 (3)	2.6 (3)	6.5 (3)	0.4 (3)
175–200	−1.9 (3)	6.8 (3)	7.2 (3)	−0.9 (3)
298–303	1.9 (3)	9.5 (3)	7.9 (3)	−1.7 (3)
403–423	3.3 (3)	9.8 (3)	8.6 (3)	−2.0 (3)
611–623	3.5 (3)	10.0 (3)	9.4 (3)	−2.2 (3)
873–903	3.1 (3)	9.5 (3)	9.7 (3)	−2.6 (3)

			Eigenvector e_i angles (°)		
ΔT (K)	e_i	α_i	$\angle$ (e_i, a^*)	$\angle$ (e_i, b)	$\angle$ (e_i, c)
10–20	e_1	−1.4 (3)	−11.7 (9)	90	101.7 (9)
	e_3	6.4 (3)	78.3 (9)	90	−11.7 (9)
36–45	e_1	−3.6 (3)	−6.1 (9)	90	96.1 (9)
	e_3	6.4 (3)	83.9 (9)	90	−6.1 (9)
70–80	e_1	−4.6 (3)	−2.3 (9)	90	92.2 (9)
	e_3	6.5 (3)	87.7 (9)	90	−2.3 (9)
175–200	e_1	−2.0 (3)	6.1 (9)	90	83.9 (9)
	e_3	7.3 (3)	96.1 (9)	90	6.1 (9)
298–303	e_1	1.5 (3)	14.7 (9)	90	75.3 (9)
	e_3	8.4 (3)	104.7 (9)	90	14.7 (9)
403–423	e_1	2.6 (3)	18.5 (9)	90	71.5 (9)
	e_3	9.3 (3)	108.5 (9)	90	18.5 (9)
611–623	e_1	2.7 (3)	18.3 (9)	90	71.7 (9)
	e_3	10.1 (3)	108.3 (9)	90	18.3 (9)
873–903	e_1	2.2 (3)	18.8 (9)	90	71.2 (9)
	e_3	10.6 (3)	108.8 (9)	90	18.8 (9)

Table 5
^{57}Fe Mössbauer parameters for $Cu_2Fe_2Ge_4O_{13}$.

T = temperature, IS = isomer shift (mm s^{-1}), QS = quadrupole splitting (mm s^{-1}), HWHM = line width expressed as half width at half maximum (mm s^{-1}), H = internal magnetic field (kOe), η = asymmetry parameter $(V_{xx} - V_{yy})/V_{zz}$; θ = angle between V_{zz} (main component of the electric field gradient) and the direction of the magnetic field (°).

T	IS	QS	HWHM	H	η	θ
295	0.398 (3)	0.697 (2)	0.130 (2)	–	–	–
260	0.423 (2)	0.709 (2)	0.138 (3)	–	–	–
200	0.456 (3)	0.700 (2)	0.130 (3)	–	–	–
170	0.473 (2)	0.706 (2)	0.131 (2)	–	–	–
150	0.480 (3)	0.709 (3)	0.132 (2)	–	–	–
130	0.488 (3)	0.710 (2)	0.132 (3)	–	–	–
120	0.494 (3)	0.711 (3)	0.133 (3)	–	–	–
110	0.497 (3)	0.711 (2)	0.134 (3)	–	–	–
100	0.499 (3)	0.712 (2)	0.135 (3)	–	–	–
90	0.501 (2)	0.711 (3)	0.138 (3)	–	–	–
80	0.505 (2)	0.709 (2)	0.138 (3)	–	–	–
20	0.519 (6)	0.700 (5)	0.174 (9)	458.4(8)	0.0	50.8 (3)

tive thermal expansion still persists at higher temperatures. Thus, for $Cu_2Fe_2Ge_4O_{13}$, we extended the temperature range and data are available between 10 and 906 K (Fig. 3; Table 3). Data obtained from X-ray diffraction experiments on single crystals and on a powder correspond well to each other. The most interesting temperature variation is displayed by the a lattice parameter (Fig. 3*a*), which shows a negative thermal expansion between 40 and 200 K, changes slope above this temperature and increases almost linearly above 300 K with temperature. The b lattice parameter (Fig. 3*b*) behaves normally, while the c lattice parameter does not show saturation at low temperature, but increases steadily with temperature (Fig. 3*c*). The monoclinic angle β first decreases up to $\sim$ 70 K and then increases with temperature (Fig. 3*d*). By comparing the relative changes of lattice parameters with respect to the values at room temperature, the smallest overall change is for the monoclinic angle, followed by the a lattice parameter, while b and c expand significantly with increasing temperature (Fig. 3*f*). The different thermal behaviour of the lattice parameters is evident from the variation of the thermal expansion tensor α_{ij} (Table 4). The three principal components of the thermal expansion tensor reflect the anisotropic low-temperature behaviour of the structure with α_1 first becoming negative and having its largest negative expansion at 75 K ($\alpha_1 = -4.7 \times 10^{-6}$ K^{-1}); above 350 K saturation to a value of *ca* +2.5 $\times 10^{-6}$ K^{-1} is found (Fig. 4*a*). The component α_2 (being parallel to the b direction) shows typical behaviour with a high-temperature saturation to a value of *ca* +9.6 $\times 10^{-6}$ K^{-1} above 350 K, and a decreasing thermal expansion towards low temperature, while α_3 shows obvious thermal expansion even at low temperatures and does not saturate at high temperatures. As temperature increases, the eigenvector values e_1 and e_3 change their orientation with respect to a^* and c, reflected by the change of the angle φ (Fig. 4*b*). At low temperatures, e_1 is parallel to the a direction within $\pm$ 5°, but it successively rotates towards the c direction with increasing temperature. Above $\sim$ 350 K insignificant alterations take place and e_1 is oriented with $\sim$ 18° to a^* (24° to a) and $\sim$ 72° to c. Inspection of Fig. 4(*c*) shows that there is no discontinuity around 40 K, which might be a sign that the thermal expansion tensor is influenced by the magnetic phase transition. The representation of the orientation quadratic viewed down $\|\boldsymbol{b}$ is shown in Fig. 5. Considering the nature of the $Cu_2Fe_2Ge_4O_{13}$ structure, the direction of greatest expansion is along $\alpha_2 \| b$ and parallel to the crankshaft-like chains of Fe^{3+} octahedra. A similar large expansion is observed between the layers of metal–cationic sites and Ge–oligomers along $\alpha_3 \| c$. Expansion

here is probably dominated by the increase of the $Fe^{3+}O_6$ polyhedra and the changes in the O—O—O bridging angles of the Ge_4O_{13} unit, which mainly influence the ***c*** dimension. Data show that along *a** (which is close to the direction of the Cu—Cu interatomic distance), there is little expansion and that this is probably strongly influenced by a low-temperature repulsion between neighbouring Cu atoms within the dimer (negative thermal expansion).

3.2.2. The Fe^{3+} site. Increasing temperature causes a smooth, almost linear increase of the average Fe^{3+}—O bond length (Fig. 6*a*). This is mainly due to the obvious alterations of the larger Fe—O6, Fe—O1 and Fe—O8 bond lengths (Figs. 2 and 6*b*; Table 4). It is observed that the longer the Fe^{3+}—O bond, the more it expands with temperature. All the highly expandable bonds involve direct contact between two neighbouring Fe^{3+} sites through the common O6—O6 edges along the *a* direction and O1—O8 along the *b* direction, respectively. Thus, it may be concluded that the obvious increase of these bond lengths is dominated by the (increasing) interatomic distance between neighbouring Fe^{3+} sites and the Fe^{3+}–Fe^{3+} repulsion along the *a* and *b* directions. Increasing temperature goes along with an increase of the BLD (Fig. 6*c*), while the ELD slightly decreases as does the ratio of $\langle e_u\rangle/\langle e_s\rangle$ as a consequence of the non-uniform change of average values of 'unshared' and 'shared' octahedral edges $\langle e_u\rangle$ and $\langle e_s\rangle$, respectively (Fig. 6*d*). Among the individual O—O edges of the $Fe^{3+}O_6$ octahedron, the largest increases with temperature are found for the O6—O7 and the O1—O8 edges. The former crosslinks Ge4 with Ge2, and the Cu site in a direction which is approximately diagonal within the *ab* plane, the latter connects two neighbouring octahedra along the *b* direction (*cis* connection), and also crosslinks the Ge4 with the Ge1 site. The large changes of these two edges are related to the fact that bond lengths at the Cu and the Ge sites do not change much; at the same time, however, the unit cell expands. As a consequence, related O—O edges have to relax. The quadratic octahedral angle variance OAV (Robinson *et al.*, 1971) decreases by $\sim 4^\circ$ between 90 and 900 K. This is further evidence that the deviation from ideal geometry for the $Fe^{3+}O_6$ octahedron decreases with increasing temperature, even if the octahedron cannot be considered to be regular even at high temperatures.

The Fe^{3+}–Fe^{3+} interatomic distance, which is parallel to the crystallographic *b* axis and which intersects the O1—O8 common octahedral edges, increases almost linearly with temperature (Fig. 6*e*). This correlates well with the obvious increase in Fe^{3+}—O1 and Fe^{3+}—O8 bond lengths, the increase of the O1—O8 octahedral edge and finally the *b* lattice parameter. At temperatures above 300 K, the Fe^{3+}—Fe^{3+} interatomic distance, pointing approximately in the *a* direction, increases with temperature at almost the same extent as the Fe—Fe distance pointing towards *b*. At temperatures below 300 K, however, there is only a small increase with temperature. This is exactly the same behaviour as in $Cu_2Sc_2Ge_4O_{13}$ (Redhammer & Roth, 2004). It is also interesting to note that the change in the Fe^{3+}—Cu interatomic distance, which again points towards *a*, is small and amounts to about a quarter of the increase in the Fe—Fe distance within the same temperature region (Fig. 6*f*). This suggests some kind

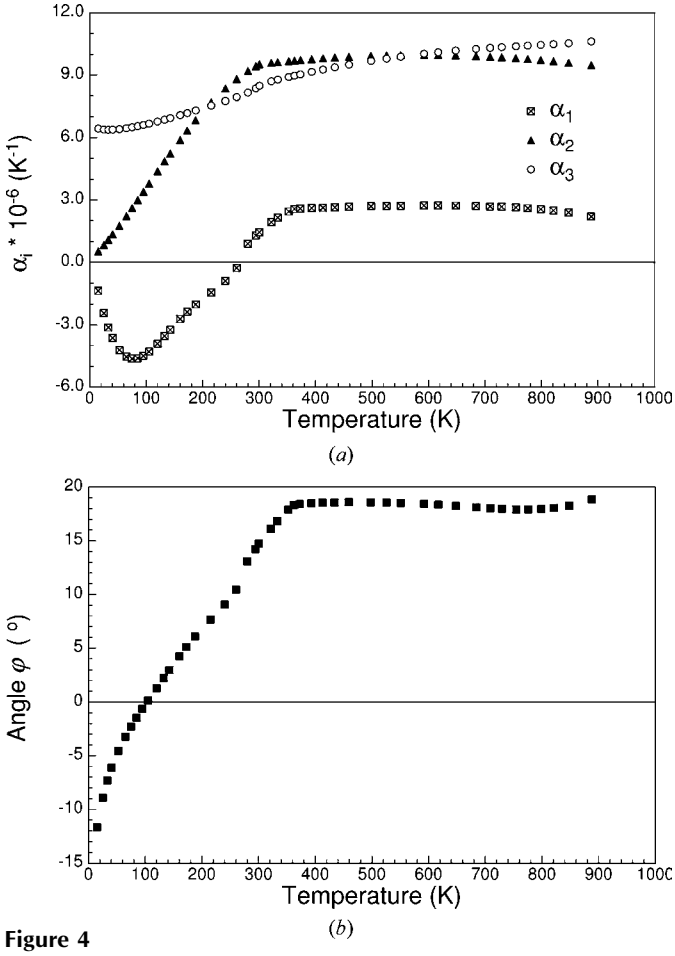

Figure 4
The temperature dependence (*a*) of the thermal expansion tensor coefficients α_{ij}, (*b*) of the magnitudes of the principal thermal expansion tensor components α_i and (*c*) of the orientation of the principal axis α_1 relative to *a** (angle φ as defined in the text).

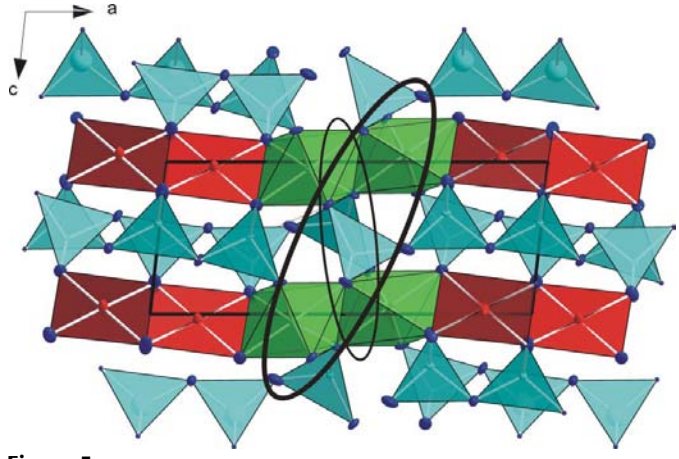

Figure 5
Thermal-dependent rotation of the eigenvectors e_1 and e_3 of the thermal expansion tensor in $Cu_2Fe_2Ge_4O_{13}$: Projection of the representational quadratic onto the *ac* plane. The thin-line ellipse represents the low-temperature tensor (10–20 K range) and the thick line the room-temperature tensor.

of (repulsion) interaction between Fe^{3+} and Cu^{2+}, which counteracts the thermal expansion of interatomic distances.

3.2.3. The Cu^{2+} site. Over the complete temperature range the average Cu^{2+}—O bond lengths remain constant within experimental error, however, individual bond lengths change significantly (Fig. 7*a*): Cu—O bond lengths to atoms O7 and O4, which are also bonded to the Fe^{3+} and Ge^{4+} sites, increase, while those bonded to Ge^{4+} and the neighbouring Cu^{2+} site decrease with increasing temperature. The anisotropic variation of the Cu bond lengths causes the BLD to increase with increasing temperature. The correlation is almost linear. For the O—O edges it can be noted that the O9—O9 edge, connecting two CuO_4 planes to dimers, decreases significantly in size above 200 K. The O4—O7 edge, which interconnects the dimer with the Fe chain tends to decrease with increasing temperature up to *ca* 300 K, beyond which it increases. For the two O—O edges, pointing in the *a* direction, the overall changes are small and do not exhibit clear trends. A prominent temperature variation is displayed by the Cu—Cu interatomic distance within the dimer: it decreases significantly with increasing temperature between 90 and 300 K. A similar observation was made for the Sc^{3+} analogue (Redhammer & Roth, 2004). Above ∼500 K, the Cu—Cu interatomic distance remains constant within experimental error. As in $Cu_2Sc_2Ge_4O_{13}$, the Cu—O9—Cu angle decreases between 90 and 300 K from 102.9 (1) to 102.4 (1)°. Above room temperature it remains constant up to 600 K, while it increases above this temperature to 102.9 (1) at 900 K. The negative expansion of the Cu—O9 bond lengths, the changes in the Cu—O9—Cu angle and the significant decrease of the O9—O9 edge of the Cu square are assumed to be a direct consequence of the behaviour of the Cu—Cu interatomic distance. It is obvious that towards lower temperatures some kind of interatomic repulsion forces between neighbouring Cu^{2+} atoms have to exist, which are most active at low temperatures. These most probably are of an electronic and/or magnetic nature. Unfortunately, the scatter in interatomic distances obtained from Rietveld refinements is so large that no valid trends can be observed. Data suggest that the negative correlation between the Cu—Cu distance and temperature still persists towards 10 K. This negative expansion of the Cu—Cu interatomic distances are assumed to be the main reason for the negative thermal expansion of the ***a*** lattice parameter below room temperature.

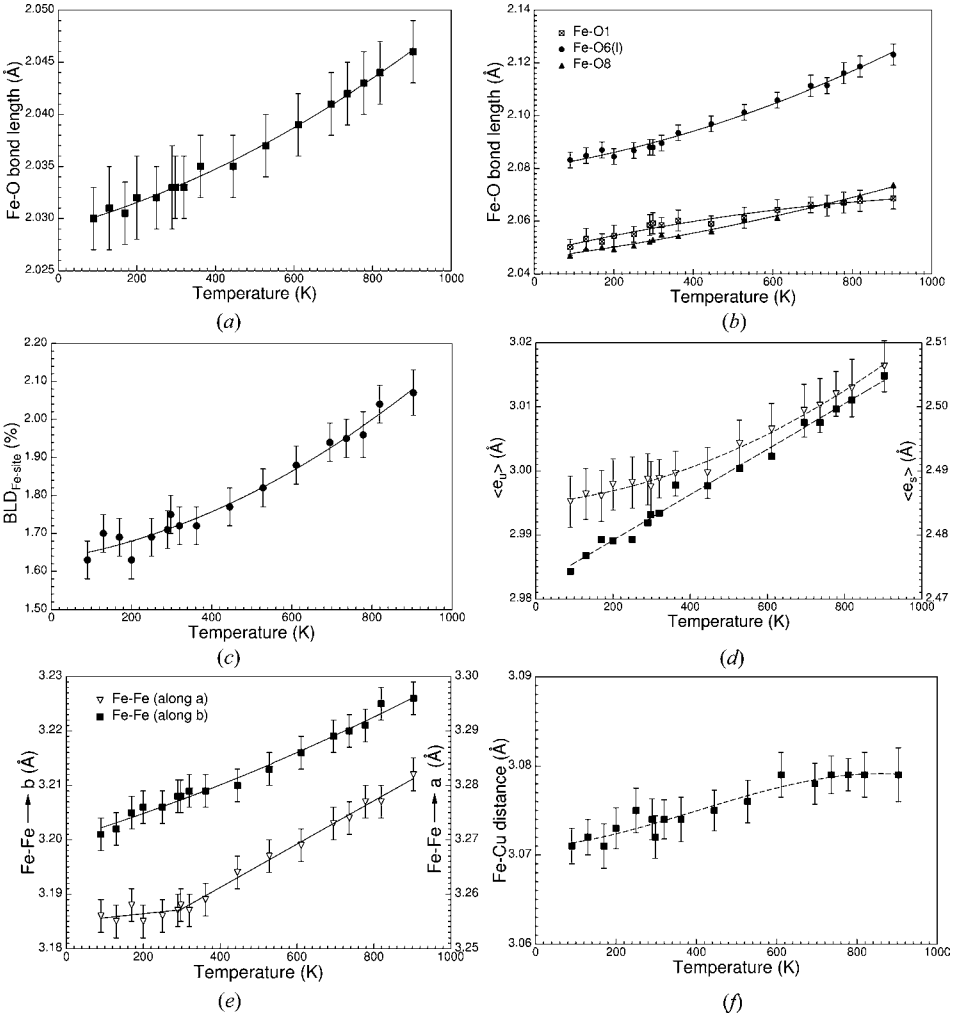

Figure 6
Variation of structural parameters of the $Fe^{3+}O_6$ octahedron between 90 and 900 K. (*a*) average Fe^{3+}—O bond length; (*b*) selected individual Fe^{3+}—O bond lengths; (*c*) bond-length distortion parameter BLD; (*d*) average of the O—O edges, shared with other topological units $\langle e_s \rangle$, right-hand scale compared with the average of the O—O unshared edges $\langle e_u \rangle$, left-hand scale; (*e*) interatomic Fe—Fe distance along the *b* axis (left-hand) and the *a* axis (right-hand scale); (*f*) interatomic distance Fe—Cu as a function of temperature; for clarity error bars are not shown for Fe—O8 in (*b*) and $\langle e_s \rangle$ in (*d*).

3.2.4. The Ge tetrahedral sites. Within the Ge_4O_{13} unit the variations of bond lengths with temperature generally are small (Fig. 8*a* and *b*). The largest changes are observed for the Ge1—O3, Ge2—O2 and Ge4—O2 bond lengths (Table 2). All these bonds are associated with O atoms, bridging the tetrahedra along the O1—O3—O5—O2 axis. While the bond lengths are fixed, several O—O tetrahedral edge lengths and bond angles alter considerably. Again these mainly involve O—O edges lying within the bridging axis of the tetramer (*i.e.* O3—O5, O5—O2 and O2—O8; Table 2) and edges bridging the roof-like Cu dimers (O4—O4, O9—O9 and O2—O7). The angles opposite these edges (Fig. 2) also change considerably. By far the largest

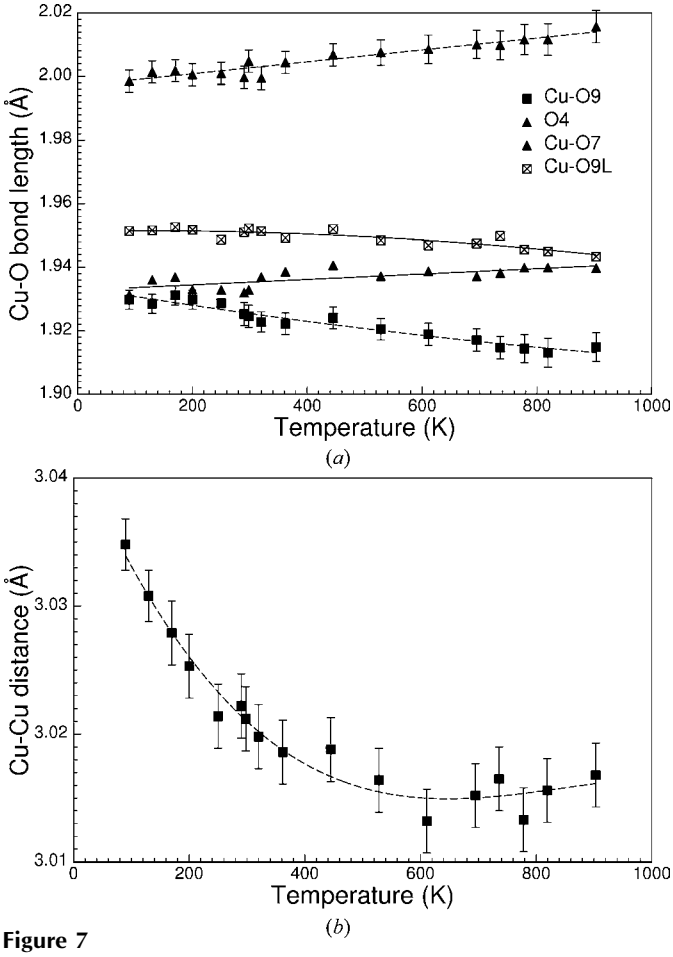

Figure 7
Cu—O bond lengths for $Cu_2Fe_2Ge_4O_{13}$ as a function of temperature (*a*) and the Cu—Cu interatomic distance within the dimer for $Cu_2Fe_2Ge_4O_{13}$ as a function of temperature (*b*).

temperature-dependent alterations concern the edges around the Ge4 site. Here it is the O2—O8 (within the tetramer axis) and O6—O6 tetrahedral edges (bridging two $Fe^{3+}O_6$ octahedra along *b*) which both decrease considerably with increasing temperature; this is behaviour which is opposite to what is normally expected. It is assumed that the thermal expansion of the crankshaft-like octahedral chain causes a decrease of the cavity between the two next-nearest neighbour octahedra along *b* into which the Ge4 tetrahedron has to fit (Fig. 2). To ensure this, some tetrahedral edges are forced to decrease with increasing temperature. Polyhedral distortion parameters remain almost constant for the Ge1 and the Ge3 site, while the tetrahedral angle variance, TAV, tetrahedral quadratic elongation, TQE, and ELD decrease with increasing temperature for the Ge2 and the Ge4 sites (Fig. 8*c* and *d*), reflecting more regular polyhedra at high temperature. Above 300 K the O1—O3—O5 bridging angles within the tetramer decrease with increasing temperature by $\sim 1°$; the O3—O5—O2 angle increases by about the same amount. The O5—O2—O8 angle shows a smooth almost linear increase with temperature and the Ge_4O_{13} tetramer becomes less bent with increasing temperature. This increase of the latter angle correlates well with the decrease of the O2—O8 and the O2—O7 bond lengths and the increase of the O2—O5 tetrahedral edge lengths with increasing temperature.

3.3. ^{57}Fe Mössbauer spectroscopy

To evaluate in more detail the nature of the magnetic transitions at 40 K and the broad maximum in magnetic susceptibility at 100 K, ^{57}Fe Mössbauer spectroscopic measurements were performed in the temperature range 80–298 K and at 20 K. At 298 K, the Mössbauer spectrum (Fig. 9*a*) consists of two symmetric resonance absorption lines which can be fitted mathematically with one Lorentzian-shaped doublet. No signs in the Mössbauer spectrum are indicative for ferrous iron. At room temperature the isomer shift with 0.398 (6) mm s^{-1} is typical for ferric iron in its high-spin configuration. The quadrupole splitting is quite large [0.697 (8) mm s^{-1}). This is further evidence that the oxygen coordination around the Fe^{3+} nucleus shows a large deviation from ideal octahedral coordination. Cooling $Cu_2Fe_2Ge_4O_{13}$ to 80 K does not alter the general appearance of the Mössbauer

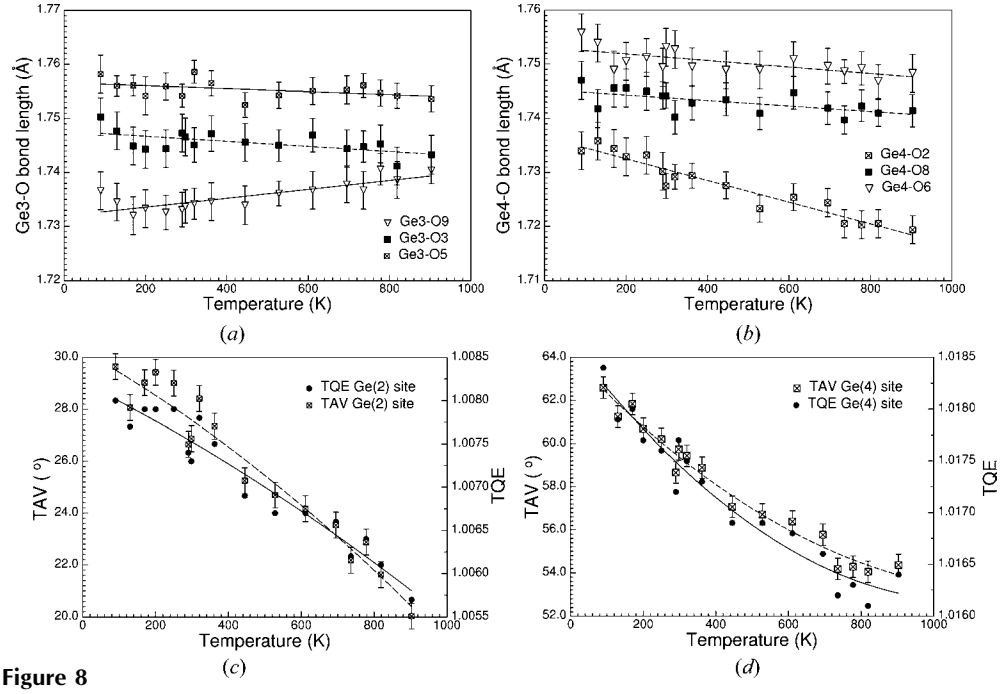

Figure 8
Ge—O bond lengths of the (*a*) Ge3 and (*b*) the Ge4 site of $Cu_2Fe_2Ge_4O_{13}$ as a function of temperature and variation of the tetrahedral angle variance TAV (left scale), and the tetrahedral quadratic elongation TQE (Robinson *et al.*, 1971; right scale) for the (*c*) Ge2 and (*d*) for the Ge4 site.

spectrum (Fig. 9*b*). It still consists of a quadrupole doublet. This means that there is no long-range magnetic order in the sample and the broad maximum in the magnetic susceptibility at 100 K may be ascribed to the Cu^{2+} sub-system.

The isomer shift of Fe^{3+} (Fig. 10*a*, Table 5) increases almost linearly with decreasing temperature. This behavior is to be expected as a consequence of the second-order Doppler shift. Owing to the $3d^5$ configuration of ferric iron (spherical charge distribution for high spin), the temperature variation of the quadrupole splitting is generally small. For the title compound, a negative correlation is observed above 100 K, *i.e.* the quadrupole splitting decreases with increasing temperature (Fig. 10*b*, Table 5). Below 100 K data points appear to exhibit a positive slope, even if the changes are within one standard deviation. This change of the sign within the data course, however, is believed to be a real effect and is further supported by the quadrupole splitting data point at 20 K. The change in slope is observed in the same temperature range as the maximum magnetic susceptibility. Also, the line width of the quadrupole doublet increases towards 100 K (Fig. 10*c*). Even if there is no long-range magnetic ordering at 100 K, Fe^{3+} quadrupole splitting as well as the line width detect some kind of changes within the local environment around the Fe^{3+} probe nuclei which correlate with the magnetic interactions within the Cu^{2+} sub-system. As ferric iron quadrupole splitting and polyhedral distortion are negatively correlated, the variation in the ferric iron quadrupole splitting as a function of temperature between 100 K and room temperature can be interpreted as a decreasing distortion of the $Fe^{3+}O_6$ octahedra when temperature is raised. This is in good correlation with the observed decrease of the polyhedral distortion parameters e_u/e_s, ELD and OAV.

When the temperature is lowered below 40 K, the Mössbauer spectrum changes drastically when a magnetically split six-line spectrum appears, *i.e.* below 40 K long-range magnetic ordering is detected. This is in excellent agreement with the results of Masuda *et al.* (2004) who determined the spin arrangement in the magnetically ordered state below 39 K using neutron diffraction experiments. Refining the magnetically split 20 K ^{57}Fe Mössbauer spectrum of the title compound (Fig. 9*c*) gives an internal magnetic field of 45.84 (8) T, which is typical for high-spin Fe^{3+} in octahedral coordination. The asymmetry parameter η, defined as $(V_{xx} - V_{yy})/V_{zz}$ is zero, *i.e.* the electric field gradient appears to be axially symmetric. The angle θ_{Hq} between the direction of the magnetic field and the main component of the electric field gradient takes a value of 51 (1)°. For the Fe sublattice Masuda *et al.* (2004) found the magnetic moments to be aligned within the *ac* plane with a slight canting along *b*. Transformed to a standard Cartesian system, linked to the crystallographic axes, the orientations of the magnetic moment $\mathbf{m}_{Fe}$ are given by (2.163, 0.121, 2.892) μ_B. Thus, the spins form an angle of $\sim 43°$ with the *c* axis and of $\simeq 53°$ with the crystallographic *a* axis. As the latter angle is similar to the θ_{Hq} angle we propose that the main axis of the electric field gradient V_{zz} may be aligned along the crystallographic *c* axis. In conclusion, ^{57}Fe Mössbauer spectroscopy shows that below 39 K a three-dimensional magnetic ordering of the title compound is present, while the maximum in the magnetic susceptibility around 100 K most probably is not influenced by the Fe^{3+} sublattice but has to be ascribed to the Cu^{2+} subsystem alone.

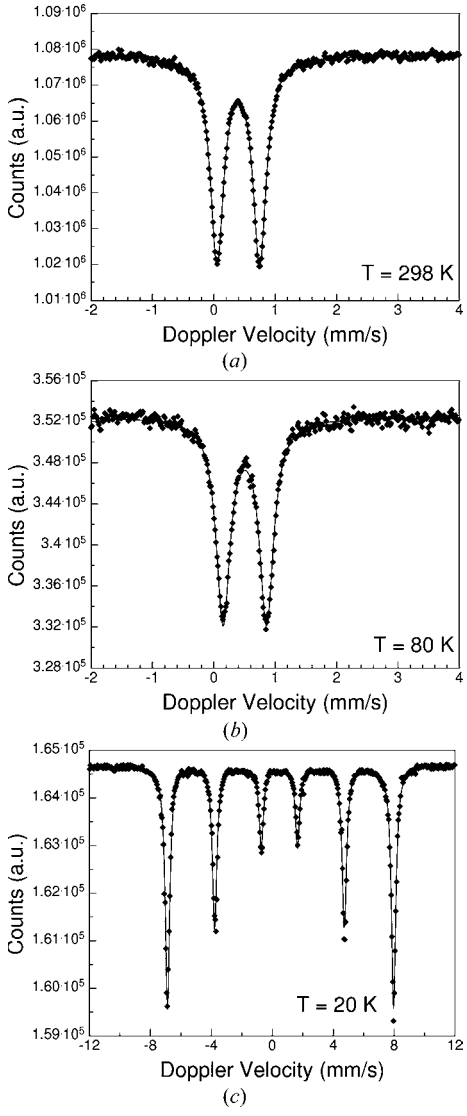

Figure 9
^{57}Fe Mössbauer spectra of $Cu_2Fe_2Ge_4O_{13}$ at different temperatures.

This work was supported by the Austrian Fonds zur Förderung der Wissenschaftlichen Forschung (FWF) under grant R33-N10 to G. J. Redhammer.

References

Benabbas, A. (2006). *Acta Cryst.* B**62**, 9–15.
Bradenburg, K. & Berndt, M. (1999). *DIAMOND*. Release 3.0. Crystal Impact GbR, Bonn, Germany.
Breuer, K. H., Eysel, W. & Berhuzi, M. (1983). *Z. Kristallogr.* **162**, 41–52.
Burns, P. C. & Hawthorne, F. C. (1996). *Can. Mineral.* **34**, 1089–1105.

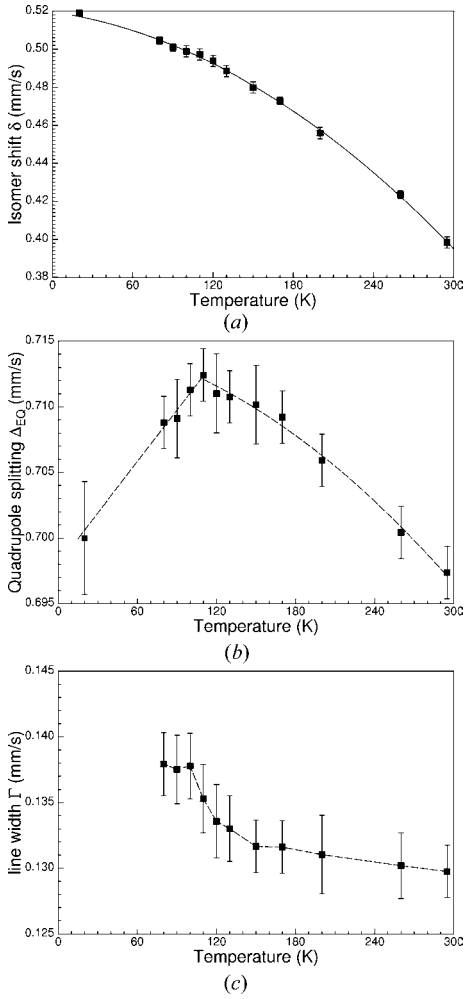

Figure 10
Variation of isomer shift δ, quadrupole splitting Δ and line width $\Gamma/2$ for $Cu_2Fe_2Ge_4O_{13}$ between 80 and 300 K.

Farrugia, L. J. (1999). *J. Appl. Cryst.* **32**, 837–838.
Hase, M., Terasaki, K. & Uchinokura, K. (1993). *Phys. Rev. Lett.* **70**, 3651–3654.
Knight, K. S., Stretton, I. C. & Schonfiled, P. F. (1999). *Phys. Chem. Miner.* **26**, 477–483.
Masuda, T., Chakoumakos, B. C., Nygren, C. L., Imai, S. & Uchinokura, K. J. (2003). *J. Solid State Chem.* **176**, 175–179.
Masuda, T., Zheludev, A., Grenier, B., Imai, S., Uchinokura, K., Ressouche, E. & Park, S. (2004). *Phys. Rev. Lett.* **93–7**, 77202–1–077202–4.
Masuda, T., Zheludev, A., Sales, B., Imai, S., Uchinokura, K. & Park, S. (2005). *Phys. Rev. B*, **72**, 094434–1–094434–8.
Paufler, P. (1997). *Physikalische Kristallographie.* Weinheim: Wiley-VCH.
Redhammer, G. J. & Roth, G. (2003). *Z. Kristallogr.* Suppl. **20**, 148–148.
Redhammer, G. J. & Roth, G. (2004). *J. Solid State Chem.* **177**, 2714–2725.
Renner, B. & Lehmann, G. (1986). *Z. Kristallogr.* **175**, 43–59.
Robinson, K., Gibbs, G. V. & Ribbe, P.-H. (1971). *Science*, **172**, 567–570.
Rodrigues-Carvajal, J. (2001). *CPD Newsl.* **26**, 12–19.
Schlenker, J. L., Gibbs, G. V. & Boison, M. B. (1975). *Am. Mineral.* **60**, 823–833.
Schonfield, P. F., Knight, K. S., van der Houwen, J. A. M. & Valsami-Jones, E. (2004). *Phys. Chem. Miner.* **31**, 606–624.
Sheldrick, G. M. (1997). *SHELXS*97 and *SHELXL*97. University of Göttingen. Germany.
Stoe & Cie (1996). *X-SHAPE* and *X-RED*. Stoe & Cie, Darmstadt, Germany.
Stoe & Cie (2002). *X-AREA*. Stoe & Cie, Darmstadt, Germany.
Toraya, H. (1981). *Z. Kristallogr.* **157**, 173–190.
Uchiyama, Y., Sasago, Y., Tsukada, I., Uchinokura, K., Zheludev, K., Hayashi, T., Miura, N. & Böni, P. (1999). *Phys. Rev. Lett.* **83**, 632–635.
Völlenke, H., Wittmann, A. & Nortny, H. (1967). *Monatsh. Chem.* **98**, 1352–1357.
Wilson, A. J. C. (1992). Editor. *International Tables for Crystallography*, Vol. C. Kluwer Academic Publishers, Dordrecht, The Netherlands.